A STUDY in HELICOPTER FUSELAGE DRAG

Andrey S. Batrakov[†], Alexander N. Kusyumov[†], Sergey A. Mikhailov[†], Vladimir V. Pakhov[†],
Artur R. Sungatullin[†], Vladimir V. Zherekhov[†] and George N. Barakos[‡]

[†]Tupolev Kazan National Research Technical University
10 Karl Marx St., Kazan 420111, Russian Federation
Email: lvi@au.kstu-kai.ru,
[‡]School of Engineers, University of Liverpool
Liverpool, L69 3GH, U.K.
Email: G.Barakos@liverpool.ac.uk

Abstract

This work investigates the contributions to the overall fuselage drag from components added to a baseline fuselage design. The ANSAT helicopter is used as an example, and this study involves both Computational Fluid Dynamics and wind tunnel experimentation. The wind tunnel data were mainly used for validation of the CFD predictions obtained and were obtained at the Kazan National Research Technical University n.a. A. Tupolev. The optimization of the rear fuselage shape for drag reduction was also addressed. The main part of the paper is, however, devoted to the analysis of drag contributions from several components of the ANSAT helicopter prototype fuselage. For this purpose, exhausts, skids and tail plane were added to the baseline shape. The results of the numerical simulations revealed that the contributions of the main fuselage, exhausts, skids and tail plane to the total airframe drag were respectively near 65%, 20% and 10%. A more streamlined shape for the fuselage reduced the fuselage drag by up to 8%.

Acronyms

CF	"clean" fuselage
SK	skids
TP	stabilizer (tail plane)
EX	exhausts
CF&EX	Fuselage with the exhausts

1. INTRODUCTION

The main goal of this paper is the investigation of different isolated helicopter fuselage configurations in terms of drag. In most cases, the isolated fuselage drag is needed as input in helicopter performance codes, and the fuselage drag and lift are important parameters for the aerodynamicists during the design phase of the aircraft [1, 2]. A key element in helicopter performance is not only the overall drag, but also, the contributions to drag of individual fuselage components. Such analysis can lead to small redesigns with large potential performance benefits [3, 4].

The current paper presents on a detailed investigation of the drag contributions of several components of the ANSAT helicopter, produced by the JSC Kazan Helicopters. The paper is divided into three sections. In the first section of the paper validation of the numerical CFD predictions is given against wind tunnel measurements for the ANSAT helicopter fuselage wind tunnel model. The measurements were obtained out at the Kazan National Research Technical University wind tunnel. The

second section shows the drag breakdown over several components of the wind tunnel ANSAT helicopter model using CFD simulations only. In the third part of the paper, questions related to the optimization of the rear fuselage for drag reduction are addressed. For this purpose, several configurations with different level of complexity were considered. Computations were performed using the multi-block structured HMB code.

The paper builds on our earlier work on the aerodynamics of several early development models of the ANSAT helicopter that are presented in references [5-8]. The contributions to the total drag of a "clean" fuselage by the front, rear and side parts were studied in reference [8] also using different turbulence models.

References [5,7] evaluated the drag of engine exhausts and helicopter skids. The multi-block structured CFD solver HMB and the unstructured commercial solver Fluent were employed. Finally, the evaluation of helicopter fuselage drag with an actuator disk was considered. Similar issues were considered in reference [6] for the ANSAT helicopter fuselage prototype. In addition, in references [5, 7, 8] the main rotor was modeled by using an actuator disc technique with uniform and non-uniform pressure distributions.

2. HELICOPTER FUSELAGE AND ADDED COMPONENTS

According to published studies the isolated fuselage drag is up to 40% of the total helicopter drag [9]. In addition, it is difficult for accurate drag estimates to be made using simple engineering methods leaving wind tunnel experimentation and Computational Fluid Dynamics as the two main sources of design data. Modeling helicopter aerodynamics with CFD requires significant computer resources. For this reason, the study of the aerodynamic interference between components of the helicopter fuselage is both difficult and important. The helicopter fuselage *F* can be divided into several parts: "clean" fuselage *CF*, skids *SK*, and stabilizer *TP*. Engine exhausts *EX* also can be considered as a separate element of fuselage. In this study, the fuselage is considered as a union of several components.

$$F=CF\&EX\&SK\&TP.$$

Fig. 1 presents the geometry of the ANSAT-P fuselage. The basic geometry without skids, tail plane etc, was provided by Kazan Helicopters.

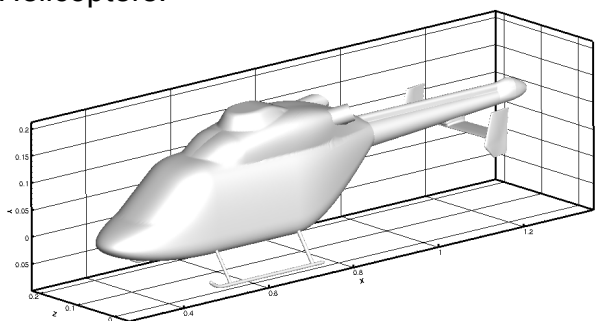

Figure 1. Geometry of the helicopter fuselage

To investigate the aerodynamic drag interference, the following method was used. First computations were performed for isolated components (e.g. skids, tail plane etc), and the baseline fuselage shape. Then these components were added to the baseline fuselage shape and computations were repeated for more complex configurations (e.g. fuselage with tail plane and skids). The drag coefficients for all cases were determined using the reference area of fuselage S_F. Then, the coefficient of interference for each element added to the clean fuselage was determined as a ratio of the drag coefficient obtained from the coupled computation over the sum of the drag coefficients of the components. For example, for a component *I*:

$$K_{CF\&I} = C_{D(CF\&I)}/(C_{D(I)} + C_{D(CF)}),$$

where (*CF&I*) corresponds to the coupled computation of the clean fuselage (*CF*) with the component (*I*) installed. If the coefficients of interference are known, the drag coefficient of a complex *CF&I* configurations can be estimated as:

$$C_{D(CF\&I)} = K_{CF\&I}\,(C_{D(I)} + C_{D(CF)}).$$

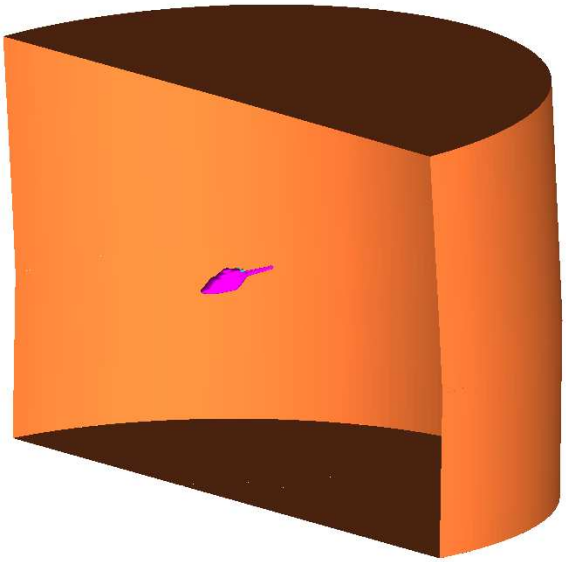

Figure 2. Overview of the computational domain

The computational domain is presented in Figure 2 and for all considered cases is a cylinder the diameter of which is 7 fuselage lengths L_F and its height is $4.4L_F$. A "Far-field" boundary condition was used for the exterior of the computational domain. A "Solid-wall" condition was used for the surface of the model.

The CFD grids were constructed using multi-block topologies generated with the ICEM-Hexa mesh generation software. Around the fuselage, the block edges were approximately orthogonal to the fuselage surface, and this was achieved using O-grids. This topology allowed for adequate resolution of the boundary layer. All computations were performed using the k-ω turbulence model.

3. COMPARISON of CFD and WIND TUNNEL DATA for CLEAN FUSELAGE WITH EXHAUSTS (*CF&EX*)

The wind tunnel model had a fuselage length of 1.8 m, and a reference area of S_F= 0.106 m^2 was used for computing the drag coefficient.

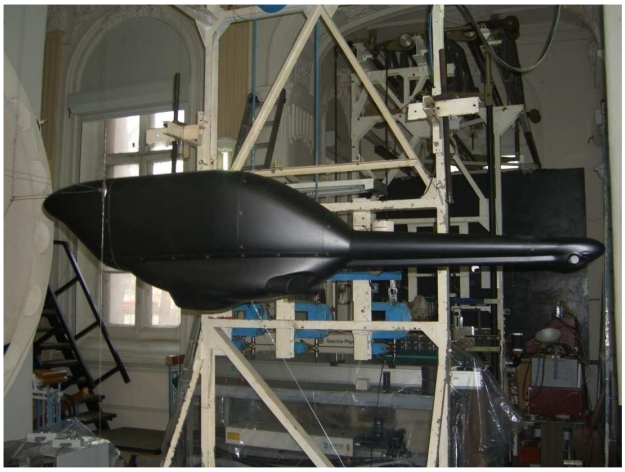

Figure 3. The ANSAT-P fuselage model in the test section T-1K wind tunnel of KAI

The conditions of the wind tunnel experiments and CFD modeling were chosen similarly to the conditions for the ANSAT-P model, discussed in references [6, 7].

For the mesh generation, the Clean Fuselage with Exhausts *CF&EX* was used as a basis (Figure 4).

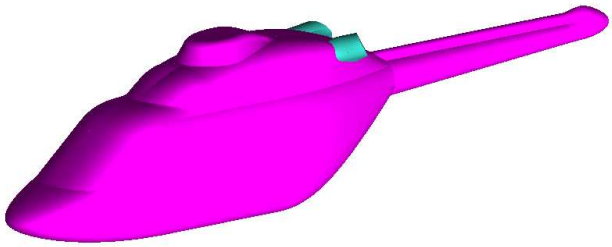

Figure 4. Fuselage with the Exhausts (*CF&EX*)

The computational grid for this model contained 964 blocks and 11.000.000 cells. The mesh edges were refined normal to the body using bi-geometric point distributions. The grid cells distribution was also refined near geometric features (near exhausts for example, as shown in Figure 5). The multi-block topology and the surface grid near the area of the exhausts are presented in Figure 6.

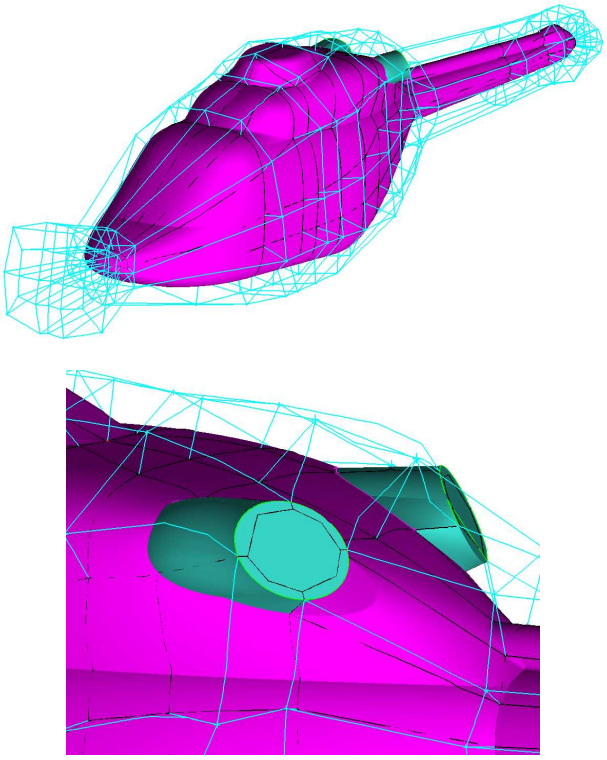

Figure 5. Multiblock topology for the *CF&EX* configuration

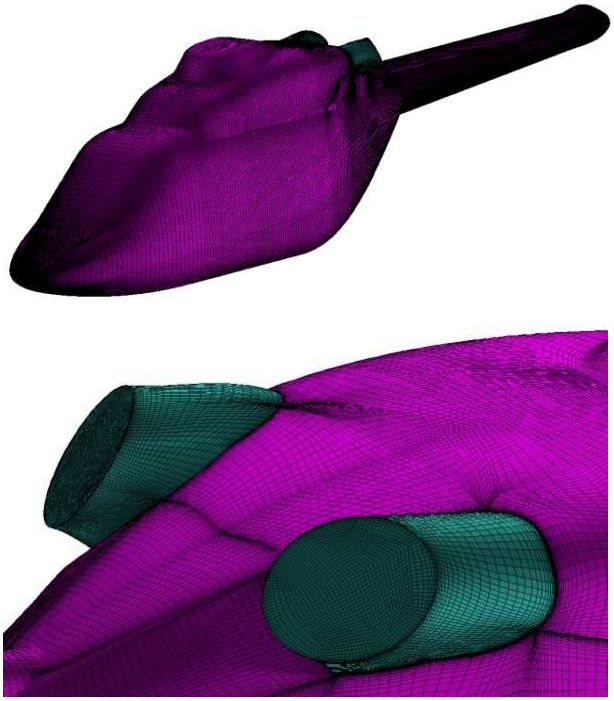

Figure 6. Surface mesh for the *CF&EX* configuration

The computational flow parameters correspond to the conditions of the wind tunnel experiments and not to a full-size aircraft. In particular, the free stream Mach number was 0.1 and the Reynolds number was of $3.2 \cdot 10^6$. Figure 7 shows the CFD predictions for the total lift and drag coefficients in comparison with the wind tunnel experiment data (the error bars correspond to the confidence intervals of the experimental measurements).

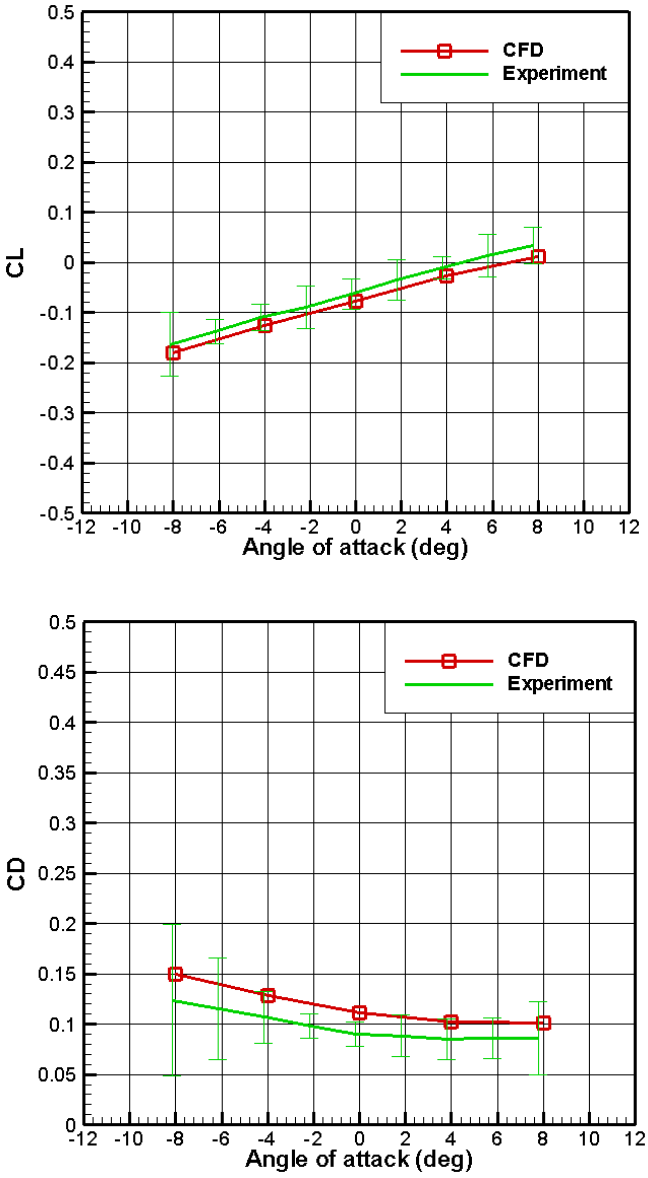

Figure 7. Lift and drag coefficients vs pitch angle: comparison between CFD and wind tunnel data for the *CF* configuration

From Figures 15 and 16 it follows that, in general, the CFD results for the ANSAT-P model are in good agreement with the experiment and within the confidence interval of the experimental data.

4. AERODYNAMIC INTERFERENCE of FUSELAGE COMPONENTS

a) Clean Fuselage layout without Exhausts (*CF*)

The initial CAD model was for the *CF& EX* configuration. Then the exhausts were deleted and covered by surfaces (Figure 8).

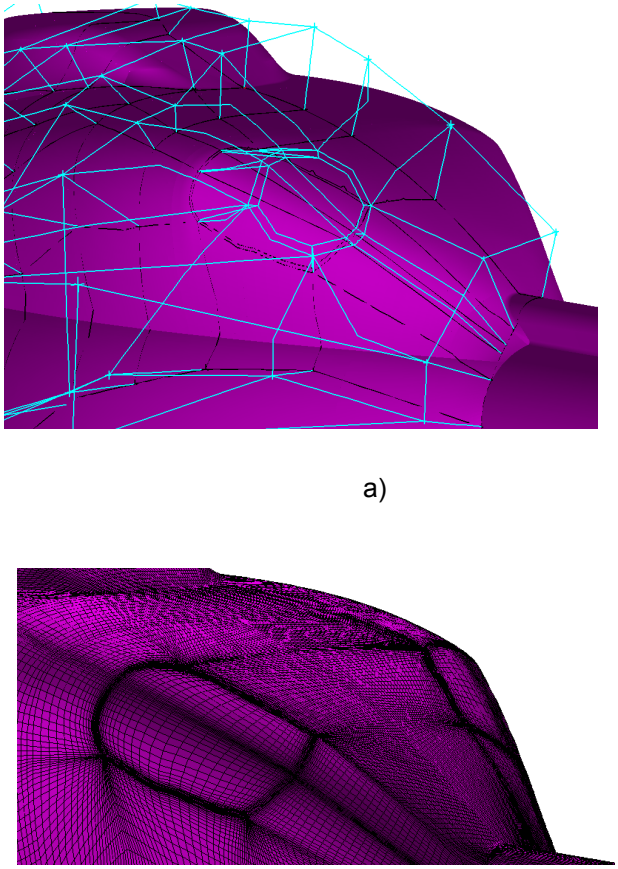

a)

b)

Figure 8. Fuselage without exhaust geometry: blocking (a); surface mesh (b)

Extra blocks for the exhausts were added to *CF* topology (Figure 8 (b)). The difference between *CF&EX* and *CF* grids are otherwise minimal. The computational grid required 974 blocks and $11.4 \cdot 10^6$ cells.

b) Fuselage configurations with and without Exhausts and added Skids

The skids SK were added to the Clean Fuselage *CF* and to the fuselage with exhausts *CF&EX*. The geometry of the skids was slightly modified to simplify the multiblock mesh generation. Crossbars were removed, and the skids were connected directly to fuselage. The CFD grid for the skids was of the O type (Figure 9).

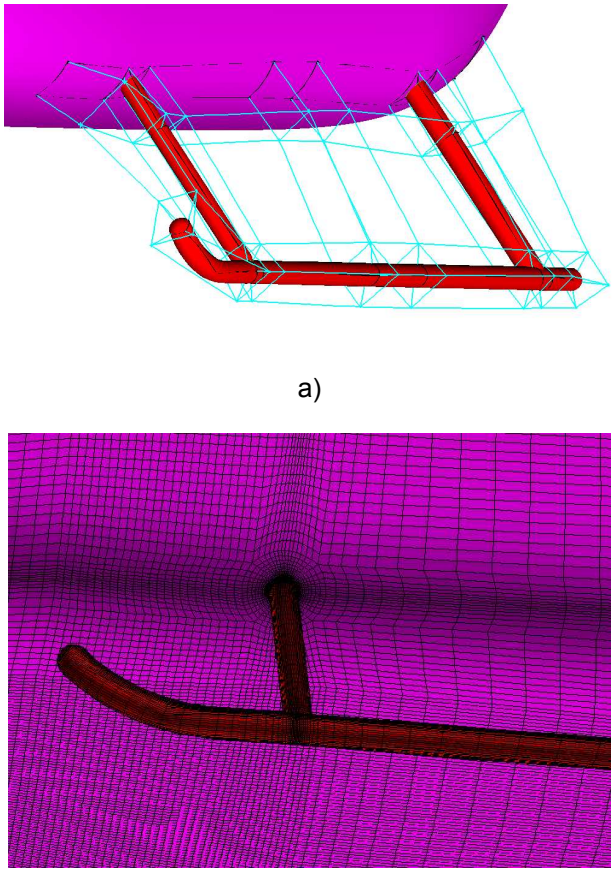

a)

b)

Figure 9. Multiblock topology for the skids (a); surface mesh (b)

The computational grid was refined in the direction normal to the skid surface. For this case the spacing of the near-wall the grid in the normal to surface direction was $3 \cdot 10^{-8} L_F$. The numbers of blocks for the *CF&SK* and the *CF&EX&SK* were 2496 and 2474 respectively; the numbers of grid cells were $23.5 \cdot 10^6$ and $23.4 \cdot 10^6$. Surface pressure coefficient distributions for the *CF&EX&SK* configuration and the velocity flow field around the skids are presented in Figure 10. Figure 10 (b) suggests that the grid resolution allows for the flow structure and separation around the skids to be well-captured.

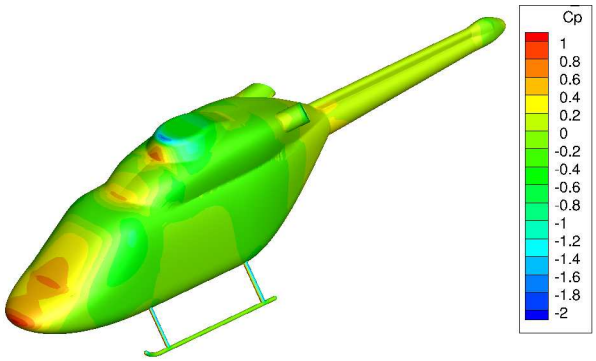

a)

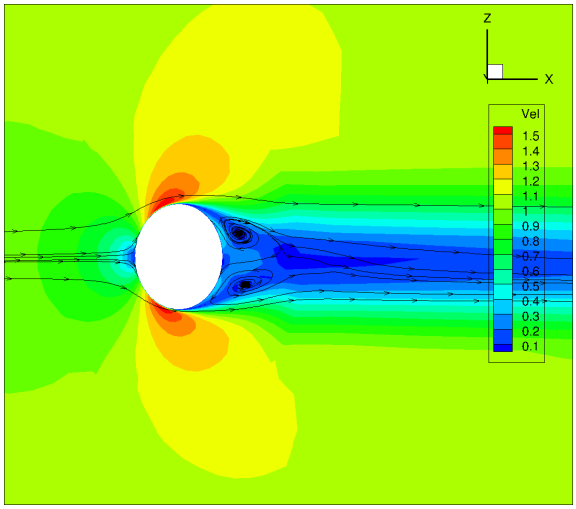

b)

Figure 10. Surface pressure coefficient on the *CF&EX&SK* (a) configuration; velocity field at the area of skids bar (b)

c) Clean Fuselage and Fuselage with Exhausts combined with Stabilizer

The stabilizer (TP) was combined with the clean fuselage and the fuselage with the exhausts. The blockings for the *CF&SK&TP* and *CF&EX&SK&TP* configurations were constructed by modifying the blockings for the *CF* and *CF&EX*. Figure 11 presents the O-grid around the stabilizer.

The CFD grids were refined near the leading and trailing edges of the stabilizer surface. For the *CL&TP* the blocks were 2444, and the number of grid cells was $24 \cdot 10^6$; for *CF&EX&TP* the blocks were 3284 and the grid cells were $25 \cdot 10^6$.

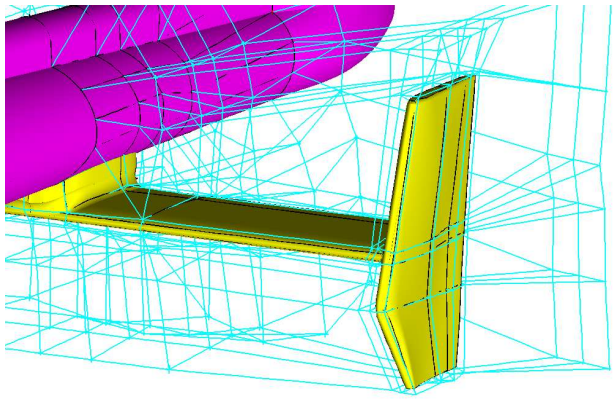

a)

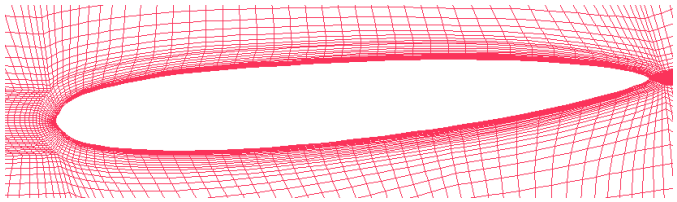

b)

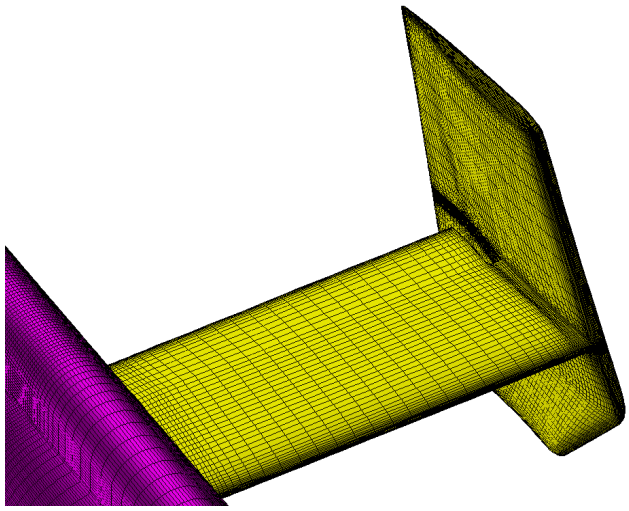

c)

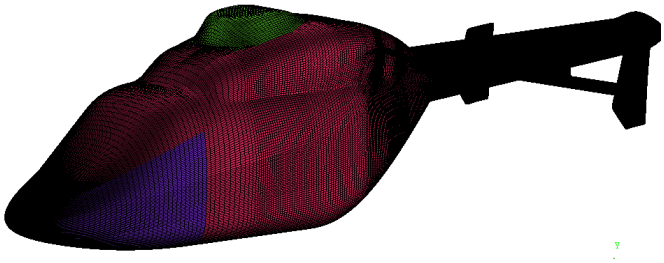

c)

Figure 11. Multiblock grid around (a) the stabilizer, and (b) the tail plane. Surface mesh on (c) the stabilizer; and (d) the CF&TP configuration

The surface pressure distribution is presented in Figure 12 and suggests that the influence of the exhausts on the tail boom and the stabilizer pressure distribution is minimal; the body surface pressure distributions for both cases look similar.

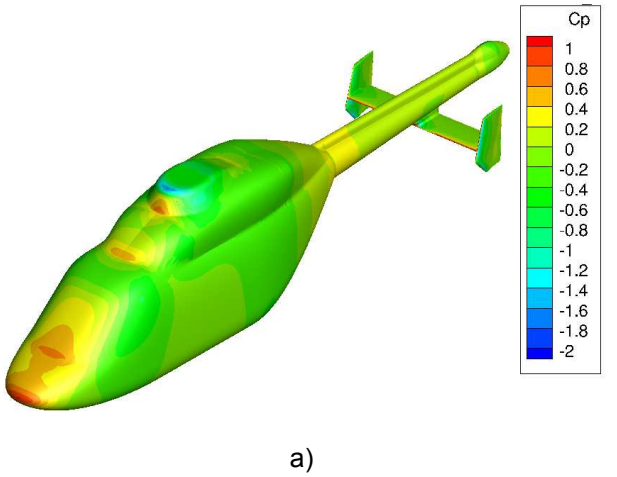

a)

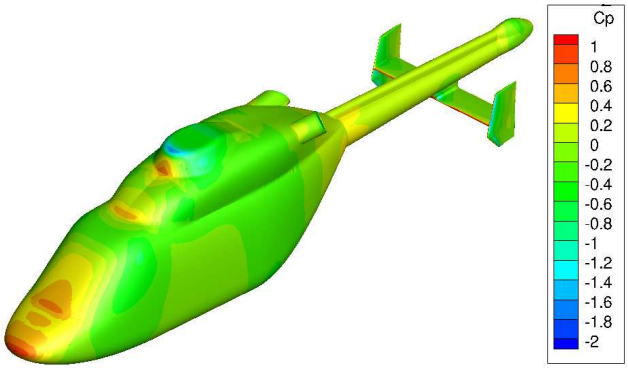

b)

Figure 12. Surface pressure coefficient distribution for *CF&TP* (a) and *CF&EX&TP* (b) layouts

d) Isolated Stabilizer (*TP*) and Skids (*SK*)

In addition to the fuselage cases, computational grids were also constructed for isolated components like the *TP* and *SK*. The geometry of the skids was smoothed in the area of the horizontal and vertical tail planes to simplify the mesh generation. The grid was refined hear the leading and tailing edges and at surface junctions. Figure 13 presents the blocking of the stabilizer and its surface mesh.

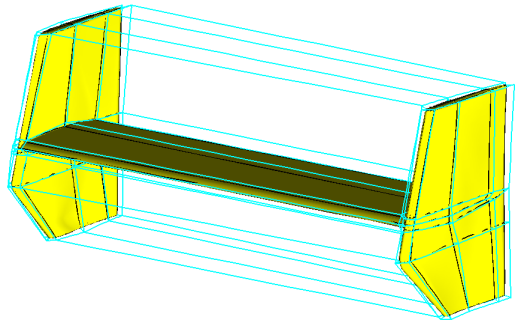

a)

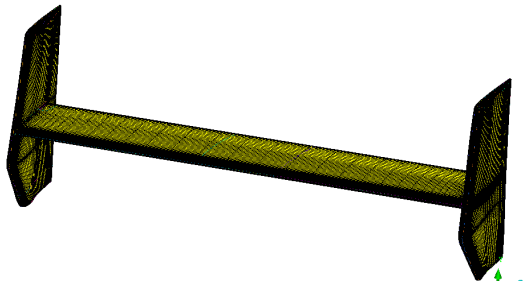

b)

Figure13. Stabilizer blocking (a) and the surface grid (b)

The number of blocks was 253, and the number of grid cells was about $4.9 \cdot 10^6$. In Figure 14 (a) the stabilizer surface pressure coefficient is shown. The negative values of the pressure coefficient on the end-plates are due to the angle these are placed at with respect to the fuselage and incoming flow.

The grid for the *CF&SK* configuration was used as a starting point for generating the grid for modeling the simplified skids. Only the isolated left part of skids was modeled with a symmetry condition to approximate configurations at zero yaw angels. For this purpose, a new grid was constructed with 363 blocks and $4.1 \cdot 10^6$ cells. In Figure 14 (b) the surface pressure coefficient distributions and symmetry plane velocity distribution are shown. Figure 14 (b) reveals different flow conditions for leading and rear skid legs: the rear leg is located within the wake of the front leg.

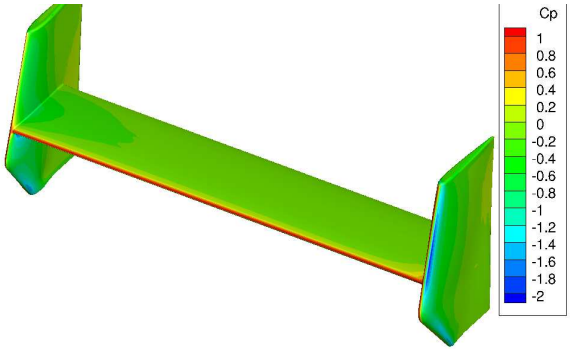

a)

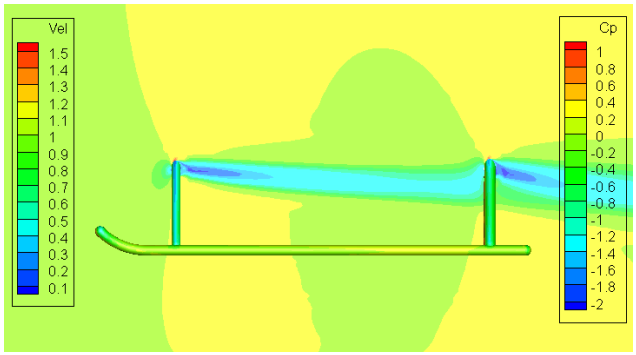

b)

Figure 14. Surface stabilizer (a) and skid (b) pressure coefficient distribution

e) Complete configuration (*CF&EX&TP&SK*)

For the flow around the complete configuration sliding grids were used. The computational domain was divided in two parts, shown in Figure 15. The first part includes the surface of fuselage (and skids) until the root of the tail boom. The tail boom and the stabilizer were included in the second part. For the first part, the grid for the *CF&EX&SK* configuration was used. For the second part, the *CF&EX&TP* configuration was used. The full grid required 3145 blocks and $31 \cdot 10^6$ cells.

The pressure coefficient distribution on the complete configuration is shown in Figure 16. From Figures 12 and 16 it follows that the pressure distribution at the tail boom area for the domain without the sliding plane (Figure 12) is similar to the surface pressure distribution with the sliding plane (Figure 16).

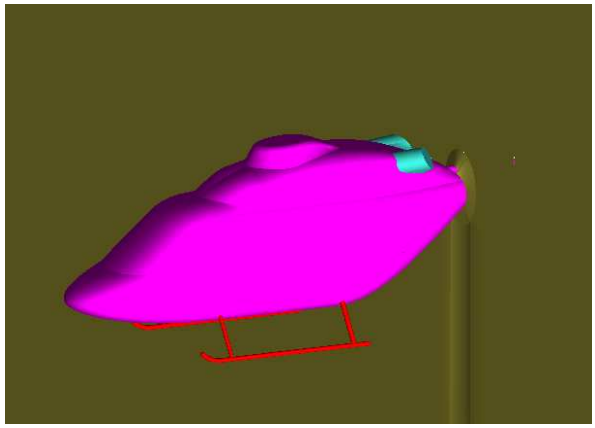

a)

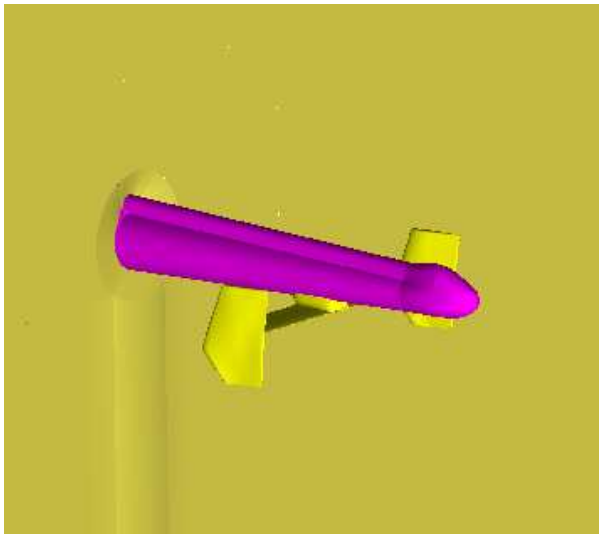

b)

Figure 15. Computational domain for the complete configuration: (a) the forward part; (b) the rear part

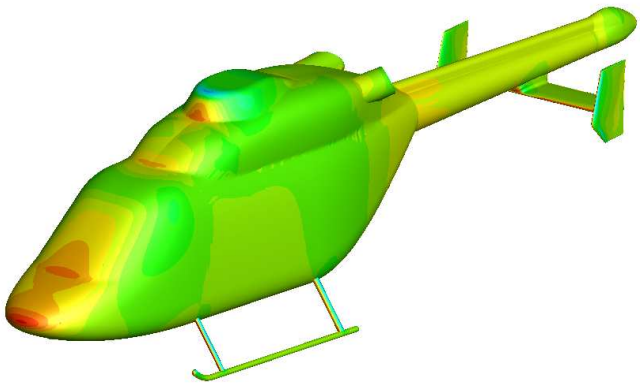

Figure 16. Surface pressure coefficient on the complete configuration

d) Analysis of aerodynamic interference

Table 1. The drag coefficients of different layouts and isolated elements for different pitch angles.

Pitch angle (α) =4 deg	Element		*CF*	*CF&EX*	*SK*	*TP*
	Isolated component		0,0837	0,0984	0,0411	0,0172
	Configuration	*CF&*	-	-	0,1304	0,0941
		CF&EX&	-	-	0,1488	0,1122
		CF&EX&SK&	-	-	-	0,1662
Pitch angle (α) =0 deg	Element		*CF*	*CF&EX*	*SK*	*TP*
	Isolated		0,0918	0,1110	0,0352	0,0186
	Layout	*CF&*	-	-	0,1299	0,0982
		CF&EX&	-	-	0,1493	0,1205
		CF&EX&SK&	-	-	-	0,1693
Pitch angle (α) =-4 deg	Element		*CF*	*CF&EX*	*SK*	*TP*
	Isolated		0,1075	0,1202	0,0384	0,0232
	Layout	*CF&*	-	-	0,1425	0,1140
		CF&EX&	-	-	0,1668	0,1408
		CF&EX&SK&	-	-	-	0,1947

Table 1 and Figure 17 show the drag coefficients for the different configurations. Table 1 also shows the values of the drag coefficients for the isolated fuselage components. The results are also presented in Figure 17. The dashed lines show the drag coefficients obtained by summing the isolated elements the drag coefficients.
From the analysis of the data, presented in Table 1 and Figure 17, it follows that there is a discrepancy between the results for the coupled configurations and the CFD computations of isolated components. This discrepancy is determined by the mutual influence of elements. The interference coefficients are presented in Figure 18.

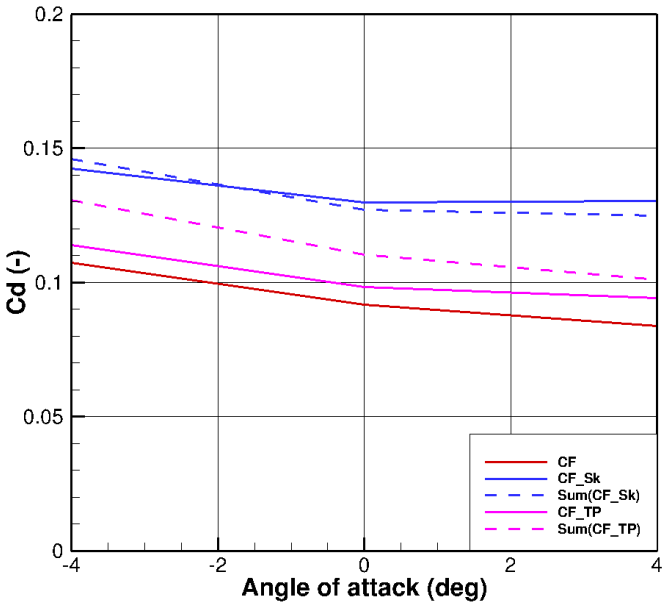

a)

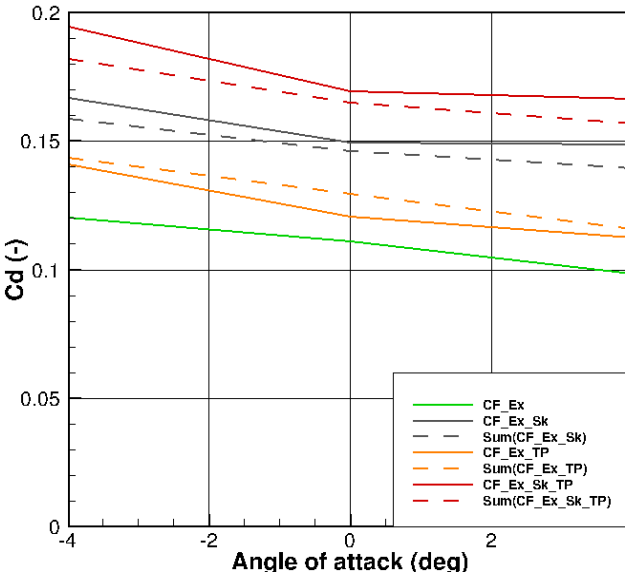

b)

Figure17. Comparison of the drag coefficient by addition of elements to the clean fuselage (a) and fuselage with the exhausts (b)

For the *CF&SK* configuration the interference effect is small. This can be explained, by the relatively small area of the fuselage/skid junction. On the contrary for the *CF&TP* configuration the interference is more significant. Thus the drag of the configuration is less than the algebraic sum of the drag of the components.

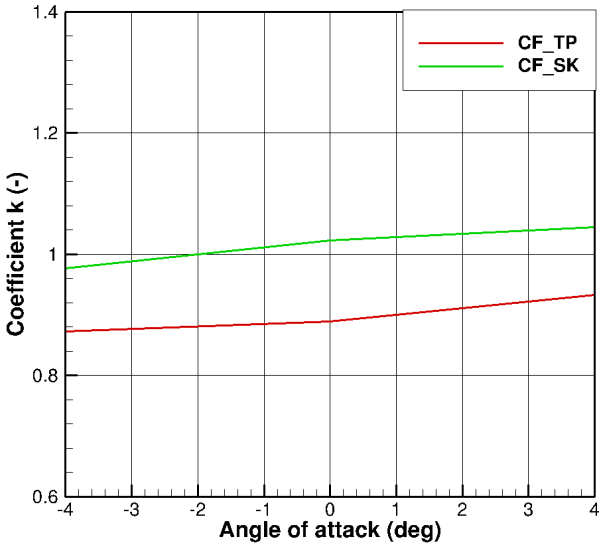

a)

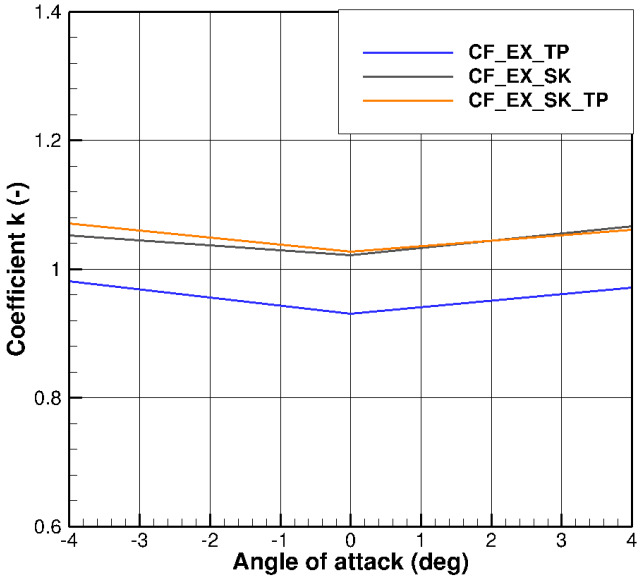

b)

Fig.18. Values of drag interference coefficients for the clean fuselage (a); and
for the fuselage with exhausts (b)

Figure 19 shows iso-surfaces for constant velocity magnitude $V=0.8V_\infty$ (V_∞ is free stream velocity) and the velocity field at the tail plane area for the *CF*, *CF&TP* and *CF&TP&SK* configurations. Figure 19 shows also that the fuselage leads to changes of the velocity magnitude and the generation of vortices at the tail plane.

For the *CF&EX&TP* configuration the interference is significant for zero degree pitch angle only. For the *CF&EX&SK* and *CF&EX&TP&SK* cases the interference is larger for no-zero pitch angles.

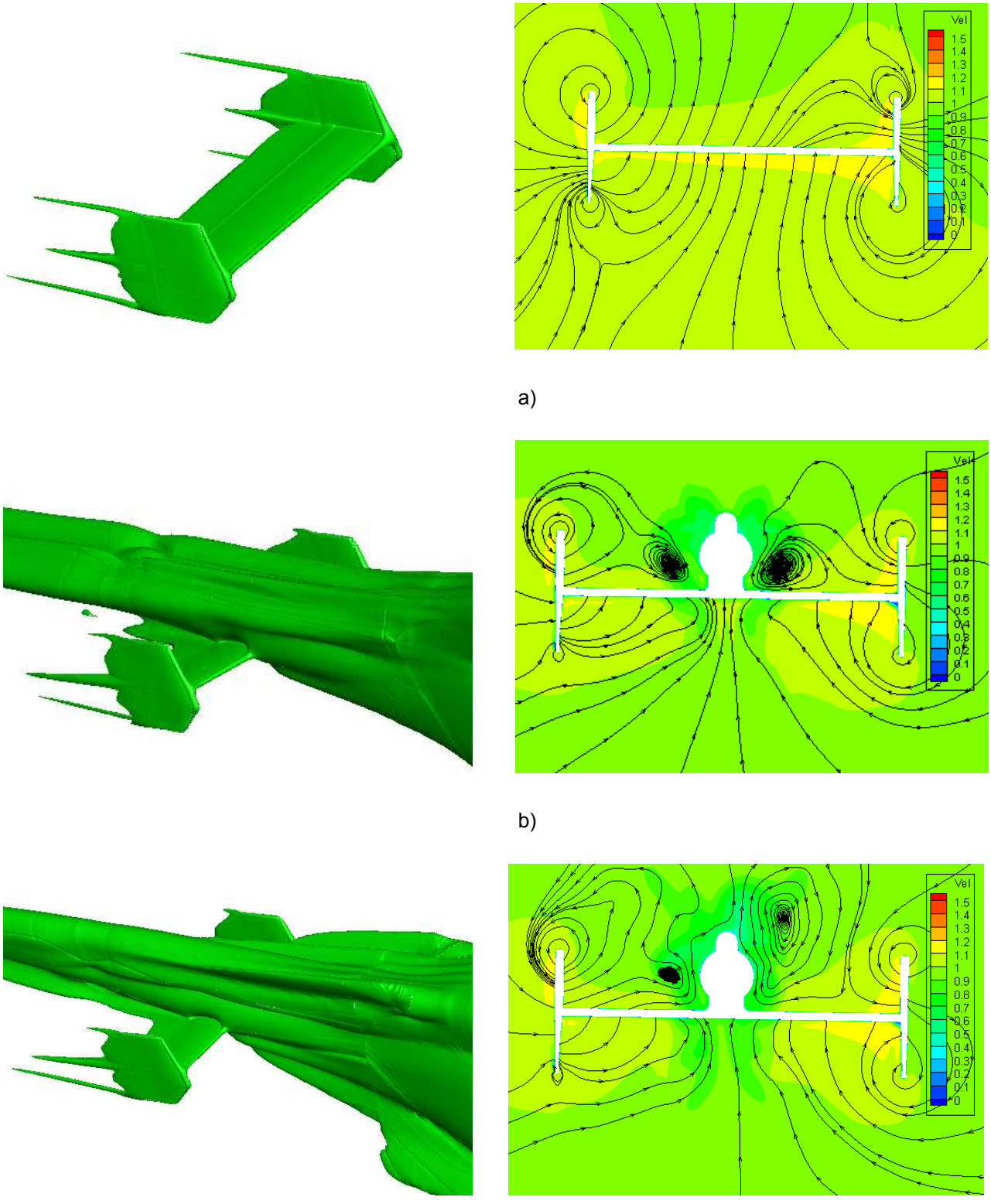

Figure 19. Iso-surfaces for constant velocity magnitude $V=0.8V_{\infty}$ and velocity field for *CF* (a), *CF&TP* (b) and *CF&EX&TP&SK* (c) configurations

5. MODIFICATION of ISOLATED ANSAT-P FUSELAGE

To estimate the influence of the rear part of the fuselage on the aerodynamic performance, several modifications were considered (Figure 20).

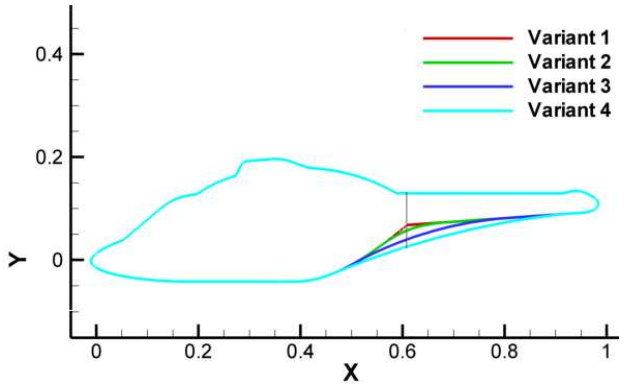

a)

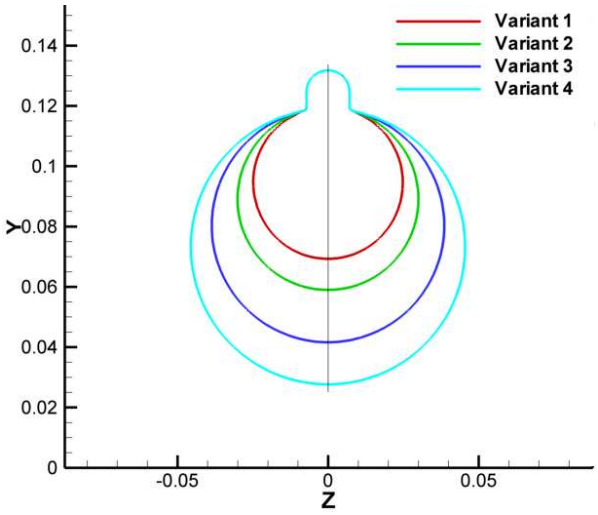

b)

Figure 20. Mid-plane shape of fuselages (a) and shape of junction line (b) between fuselage and tail boom

Figure 20 (a) presents variants of the fuselage mid-plane shape. Also the cross-sectional shape of the tail boom at the junction with the rear part of fuselage is segmented in cylinders and shown in Figure 20 (b).
A comparison of the mid-plane velocity field for the different variants of fuselages is presented in Figure 21. A more streamlined rear part leads to reduced separation area and fuselage drag coefficient.

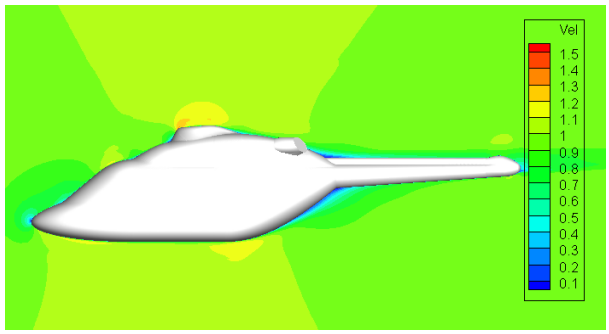

a)

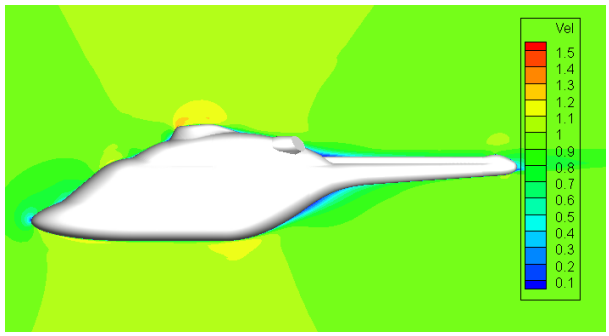

b)

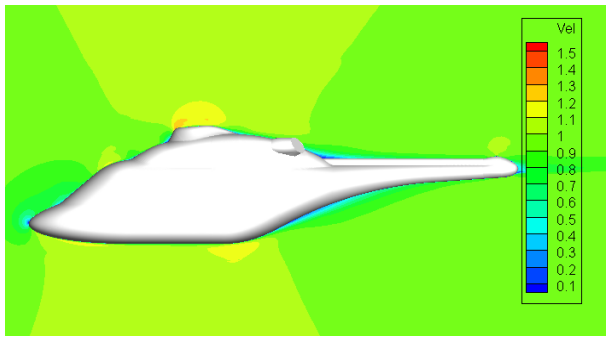

c)

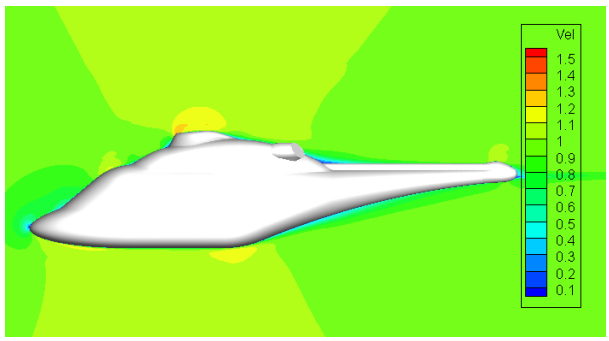

d)

Figure 21. CFD prediction of mid-plane velocity field for (a) variant1, (b) variant2, (c) variant3 and (d) variant4 fuselages at α=0 degrees

Figure 22 shows a comparison of the drag coefficient values for the variants of the fuselage shape.

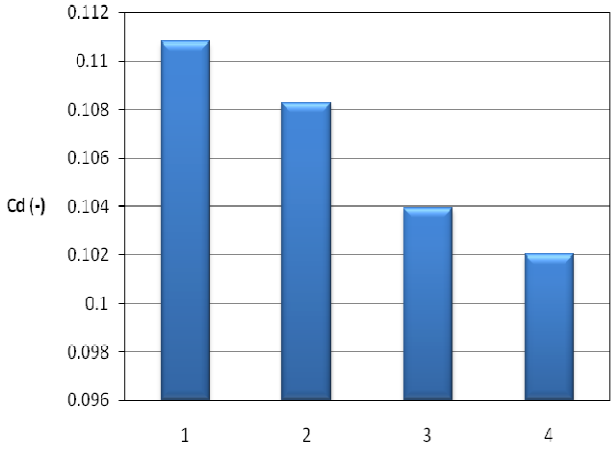

Figure 22. Drag coefficient for different variants of fuselage shape at α=0 degrees

Figure 22 a comparison of the drag coefficient values for the variants of the fuselage and shows that a more streamlined shape of the fuselage rear allows for a reduction of the drag coefficient by up to 8%.

6. CONCLUSIONS and FUTURE WORK

The flow around the idealized fuselage of the ANSAT helicopter was analyzed, and the experimental values of drag and lift coefficients were compared with CFD data. The flows around several configurations with different levels of complexity were modeled. Computations were performed using the multi-block structured HMB solver of Liverpool University. As can be seen in Table 1, the drag of the components, adds to the baseline (*CF*) values over 80% extra when exhausts (*EX*), skids (*SK*), and tail plane (*TP*) are considered.

To investigate the reduction of the drag of the rear part of fuselage CFD simulations of modified fuselages were conducted. For the ANSAT-P fuselage the more streamlined shape reduced the fuselage drag by up to 8%.

Recent researches revealed that the agreement between the experiment and CFD for the ANSAT fuselage can be improved using refined grid in the direction to surface fuselage normal. Therefore, the problem of the helicopter fuselage drag will be revisited also using optimization theory in a combination with CFD modeling, and finer computational grids.

ACKNOWLEDGMENTS

This work is supported by the “Leading Scientist” grant of the Russian Federation, under order 220 of the Russian Ministry of Education. The authors would like to acknowledge the Kazan Helicopter Plant for providing the initial fuselage shapes for this research.

REFERENCES

1. A. D´Alascio, K. Pahlke, and F. Le Chuiton, “Application of a Structured and an Unstructured CFD method to the Fuselage Aerodynamics of the EC145 Helicopter”, Prediction of the Time Averagedd Influence of the Main Rotor, European Congress on Computational Methods in Applied Sciences and Engineering, ECCOMAS 2004 Jyväskylä, 24—28 July 2004.

2. F. Le Chuiton, A. D'Alascio, G.N. Barakos,R. Steijl, D. Schwamborn, and H. Ludeke, “EC145 Helicopter Fuselage - An Industrial Case”, in: DESider - A European Effort on Hybrid RANS-LES Modelling, W. Haase, M. Braza, A. Revell (Eds.), Notes on Numerical Fluid Mechanics and Multidisciplinary Design, Vol. 103, pp. 250-260, Springer Verlag, 2009.

3. S. Schneider, S. Mores, M. Edelmann, A. D'Alascio, D. Schimke, "Drag Analysis for an Economic Helicopter", 37 European Rotorcraft Forum, Galarate, Italy, 2011,.

4. Q. Zhang, L. Jen-Der and W. Jan-Hendrik, "An Adjoint-based Optimization Method for Helicopter Fuselage Backdoor Geometry", 36th European Rotorcraft Forum, Paris, France, 2010.

5. A.N. Kusyumov, S.A. Mikhailov, E.I. Nikolaev, N.A. Shilova , A.O. Garipov, "Simu-

lation of Flow around the Fuselage of “ANSAT” Helicopter", ASME 2011 International Mechanical Engineering Congress & Exposition IMECE2011, Denver, Colorado, USA, 2011.
6. V. Pakhov, M. Valiev, V. Zherekhov, L. Makarova, A. Kusuymov and George Barakos, "Creating a Database for Validation of Predictive Methods for Rotorcraft", 47th International Symposium of Applied Aerodynamics, Paris, 2012.
7. A.N. Kusyumov, S.A. Mikhailov, E.V. Romanova, A.O. Garipov, E.I. Nikolaev, Barakos G., "Simulation of Flow around Isolated Helicopter Fuselage", EFM 2012 conference, Hradec Kralove, Czech. Republic, 2012.
8. A. Kusyumov, S. Mikhailov, A. Garipov, E. Nikolaev, Barakos G., "CFD Simulation of Fuselage Aerodynamics of the “ANSAT” Helicopter Protype", Transactions on Control and Mechanical Systems, 2012, Vol. 1, No 7, pp. 318 – 324.
9. M. Grawunder, R. Reß, C. Breitsamter, N.A. Adams, “Flow Characteristics of a Helicopter Fuselage Configuration Including a Rotating Rotor Head”, 28th International Congress of the Aeronautical Sciences. Brisbane, Australia, September, 2012.